ACS Catalysis

pubs.acs.org/acscatalysis Research Article

Subnanometer Cu Clusters on Porous Ag Enhancing Ethanol Production in Electrochemical CO_2 Reduction

Jiwon Park, Chaehwa Jeong, Moony Na, Yusik Oh, Kug-Seung Lee, Yongsoo Yang,* and Hye Ryung Byon*

Cite This: *ACS Catal.* 2024, 14, 3198–3207 Read Online

ACCESS | Metrics & More | Article Recommendations | Supporting Information

ABSTRACT: Controlling the electrochemical CO_2 reduction process for multicarbon production is challenging. Ethanol is typically produced with lower selectivity compared to ethylene. In addition, ill-defined catalytic active sites and elusive mechanisms of C−C coupling further hinder the enhancement of ethanol generation. Here, we carefully regulated the quantity of the Cu atoms and deposited them onto a Ag inverse-opal structure (AgIOs) using the pulse-electrodeposition method. Subnanometer Cu clusters demonstrated a 2.5 times higher Faradaic efficiency for ethanol production compared to that for ethylene at −1.05 V vs RHE. Conversely, as the size of Cu increased to nanometers, ethylene became the dominant product. Excessive adsorption of CO on Cu clusters, which migrates from the Ag surface, is attributed to the improved ethanol production. Abundant Ag/Cu boundaries and adjacent spacing between Ag and Cu clusters may enhance the surface migration of CO. In contrast, the preferential site-selective CO adsorption on large Cu nanoparticles is associated with solution-mediated CO migration. *Operando* shell-isolated nanoparticle-enhanced Raman spectroscopy (SHINERS) revealed a high coverage of the CO on the Cu clusters. The initial intermediate *OCCOH by C−C coupling appeared for both Cu clusters and nanoparticles. However, Cu clusters accommodated more carbonaceous intermediates, highlighting the critical role of CO and intermediate coverages on Cu in ethanol production.

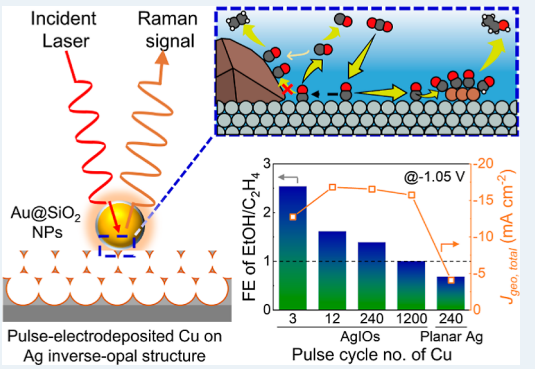

KEYWORDS: *CO_2 reduction, Cu cluster, Cu nanoparticle, inverse opal structure, operando electrochemical probe, Raman spectroscopy, SHINERS*

INTRODUCTION

A significant challenge in mitigating climate change is the elimination of emitted carbon dioxide (CO_2) gas. In addition, converting CO_2 gas into industrial resources is advantageous for the creation of new value-added materials. The electrochemical CO_2 reduction (e-CO_2R) technique is a useful method performed at room temperature and ambient conditions, and catalyst designs produce various reduction products, such as carbon monoxide (CO), methane (CH_4), ethylene (C_2H_4), and ethanol (EtOH).[1] The latter C_2 species comprising two carbons are more desired as expensive industrial resources than C_1. However, the selectivity for targeting C_2 species has generally been low compared to that of CO due to complicated electrochemical and chemical processes, e.g., C−C coupling. The fundamental understanding of the key active sites of catalysts and detailed mechanisms also remains to be resolved.[2,3]

Cu is the most widely used and effective catalyst to facilitate C_2 products in aqueous media.[4,5] By designing the crystal structures, oxidation states, and defect sites of Cu, the Faradaic efficiency (FE) of C_2H_4 was improved to ∼84.5%.[6−9] In contrast, improving EtOH selectivity remains challenging despite its better affordability for the industry.[10−12] It is presumably attributed to the thermodynamically favorable C_2H_4−forming pathway on Cu.[13] Recently, Cu in tandem with Au,[14,15] Ag,[16−19] or Zn[20] showed better FE of EtOH. In particular, Ag is an excellent CO supplier at a high cathodic potential, and CO migration increases *CO coverage on Cu, where the asterisk symbol indicates surface adsorption.[21] It suggests the extended accessibility of the Cu surface including the thermodynamically unfavorable sites, which may provide a new pathway to EtOH production. In addition, plausible active sites, including edges of Cu cubes[22] and Cu−Ag phase boundary,[23] were demonstrated. However, despite many studies on tandem catalysts, the origin of preferential EtOH production has not yet been conclusive. Accordingly, the lack of delicate tandem catalyst designs also often led to the

Received: July 27, 2023
Revised: January 6, 2024
Accepted: February 2, 2024
Published: February 14, 2024

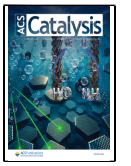

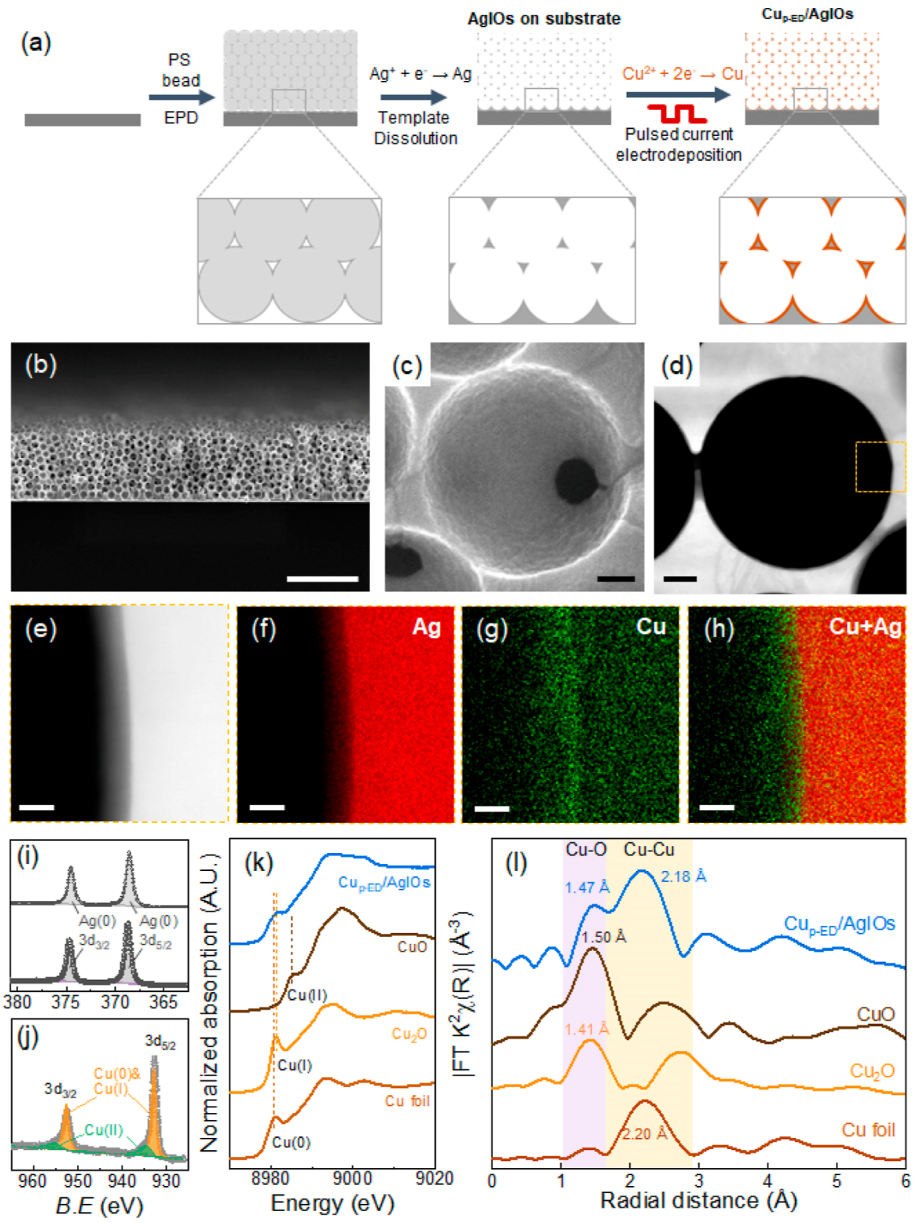

Figure 1. Fabrication and characterizations of $Cu_{p\text{-}ED}(240)$/AgIOs. (a) Schematic illustration of the $Cu_{p\text{-}ED}(240)$/AgIOs fabrication. EPD indicates electrophoretic deposition. (b) Cross-sectional SEM, (c) high-magnification SEM, and (d) HAADF−STEM images of $Cu_{p\text{-}ED}(240)$/AgIOs. The scale bars are (b) 5 μm and (c,d) 100 nm. (e) High-magnification HAADF−STEM image of the dashed-box region in (d) and simultaneously acquired EDS elemental mapping images of (f) Ag, (g) Cu, and (h) overlaid Ag and Cu. Note that the net intensity maps in (f−h) are normalized for each element to better visualize the Cu layer deposited on the Ag surface, and the maps do not directly represent the atomic fraction. The scale bars are (e−h) 10 nm. (i,j) XPS of $Cu_{p\text{-}ED}(240)$/AgIOs in the (i) (bottom) Ag 3d and (j) Cu 2p binding energy regions. The top spectrum in (i) was AgIOs. (k,l) Ex situ XAFS spectra along with references of CuO, Cu_2O, and Cu foil. (k) Cu *K*-edge XANES spectra and (l) k^2-weighted Fourier transform EXAFS spectra.

unexpected inferiority of EtOH. For example, large Cu particle sizes (hundreds of nanometers to microns) and relatively small Ag surfaces formed C_2H_4 or CH_4 rather than EtOH.[24−26] Thus, it necessitates subnanometer/atomic level control of Cu and Ag sizes and Cu−Ag boundary.

Upon well-defined catalyst structures, the main pathways for C−C coupling should be addressed. The *CO−*CO or *CO−*CHO coupling has been widely accepted as the plausible C_2-forming route.[6] Cu-based catalyst covered by nitrogen-doped carbons showed imperative C−C coupling processes and stabilizing intermediates such as $*CH_2CHO$ and HOCCH* to determine EtOH production.[27,28] In comparison, recent computational simulations and experimental methyl halide isotope tests suggested a possible route to $*CO−*CH_x$ coupling to prepare EtOH.[29,30] The key intermediates to be EtOH have still been debated and rarely observed under *e*-CO_2R conditions.

Here, we controlled Cu size as a subnanometer on a porous Ag substrate to investigate the critical parameters for EtOH production. Using well-ordered Ag inverse opal structures (AgIOs), the pulse-electrodeposition (p-ED) technique[31−33] finely regulates the quantity of Cu deposition with uniform coverage. Referring to previous studies of IOs,[34,35] our fabricating method prevented AgIOs delamination from the

https://doi.org/10.1021/acscatal.3c03469
ACS Catal. 2024, 14, 3198−3207

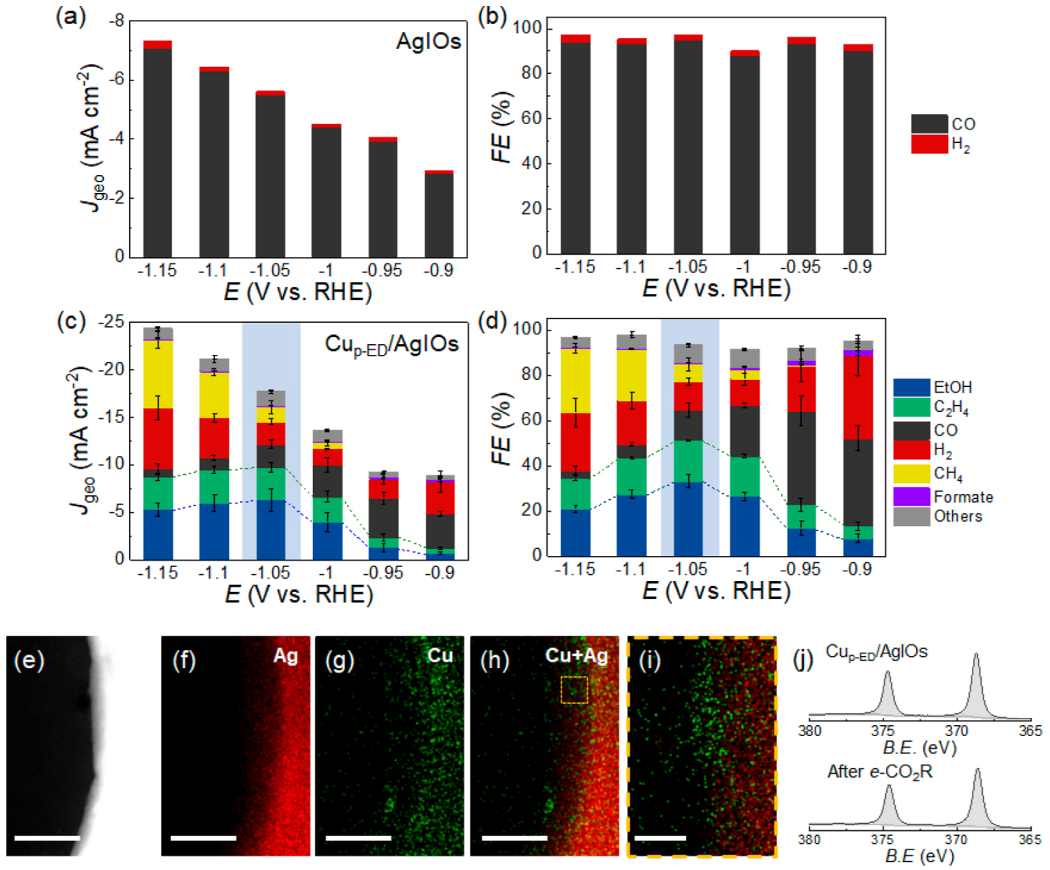

Figure 2. Characterizations of AgIOs and $Cu_{p-ED}(240)$/AgIOs for *e*-CO_2R in CO_2-saturated 0.2 M $KHCO_3$ solution. (a–d) Potential-dependent geometric partial current density (J_{geo}) for (a) AgIOs and (c) $Cu_{p-ED}(240)$/AgIOs, and FE of (b) AgIOs and (d) $Cu_{p-ED}(240)$/AgIOs. Error bars in (c,d) are standard deviations for experiments with three independently measured $Cu_{p-ED}(240)$/AgIOs samples. (e) HAADF image of the $Cu_{p-ED}(240)$/AgIOs and (f–h) simultaneously acquired EDS elemental mapping images of (f) Ag, (g) Cu, and (h) both Cu and Ag after 3 h of *e*-CO_2R at −1.05 V. The scale bars of (e–h) indicate 50 nm. (i) A high-magnification EDS elemental mapping image of the dashed box in (h). The red and green indicate Ag and Cu, respectively, and the scale bar is 5 nm. Note that the net intensity maps in parts (f–i) are normalized for each element to better visualize the segregation of Cu, and the maps do not directly represent the atomic fraction. (j) XPS spectra of Ag 3d BE regions for (top) as-prepared $Cu_{p-ED}(240)$/AgIOs (same as Figure 1i bottom spectrum) and (bottom) after *e*-CO_2R.

substrate, which allowed for successful bimetallic Cu/AgIOs with ∼6 nm thick Cu layer by p-ED. During *e*-CO_2R, Cu segregated but did not form an alloy with Ag. Subnanometer Cu clusters from small depositing quantities significantly improved the FE of EtOH compared to that of C_2H_4. With increasing Cu quantity forming nanoparticles (NPs), the FE of C_2H_4 was increased. *Operando* electrochemical shell-isolated NP-enhanced Raman spectroscopy (SHINERS) demonstrated *OCCOH as the initial intermediate of the C–C coupling for both Cu clusters and NPs. However, Cu clusters exhibited higher CO and carbonaceous species coverages than Cu NPs, suggesting a pivotal role of dense intermediates in forming EtOH.

RESULTS AND DISCUSSION

Ultrathin Cu/porous Ag frameworks were prepared by pulsed Cu electrodeposition on AgIOs (further details are provided in the Experimental section in the Supporting Information). Briefly, polystyrene (PS) beads [diameter (d) = 600 nm] were stacked with a hexagonal close-packed structure on an Au-coated Si wafer (Figure 1a).[34,36] After the deposition of Ag and PS removal (Figure S1), we confirmed no delamination of AgIOs from the substrate. Subsequently, Cu layer was plated on these AgIOs using the p-ED technique. Uniform Cu nuclei were formed by a 10 ms pulse with a current density of −100 mA cm^{-2}, followed by resting for 4.99 s at the open-circuit potential (OCP). This process was repeated 240 times to develop a Cu layer,[37−39] and the complete structure is indicated as $Cu_{p-ED}(240)$/AgIOs.

The $Cu_{p-ED}(240)$/AgIOs was composed of 7–8 layers of spherical pores (d = 600 nm) with a framework thickness of ∼4.5 μm, as shown in the cross-sectional scanning electron microscopy (SEM) image (Figure 1b). The pores were interlocked, and the inner spaces were connected through small holes (d = ∼150 nm, black spheres in Figure 1c). Grazing-incidence X-ray diffraction (GIXRD) identified 111 and 200 reflections of metallic Ag with a face-centered-cubic structure (Figure S2). As Cu character could not be detected in GIXRD, the presence of the Cu layer was verified by high-angle annular dark-field–scanning transmission electron microscopy (HAADF–STEM) together with STEM-based energy-dispersive X-ray spectroscopy (STEM–EDS, Figure 1d–h). HAADF–STEM images show even Cu layers, and their thickness (t) estimated from multiple areas was 5.7 ± 2.9 nm. X-ray photoelectron spectroscopy (XPS) demonstrated phase-segregated Cu and Ag without forming CuAg alloy, as shown in no Ag peak shift before and after p-ED Cu (Figure 1i). The Cu/Ag atomic % on the surface was 6.0/15.7, as

https://doi.org/10.1021/acscatal.3c03469
ACS Catal. 2024, 14, 3198−3207

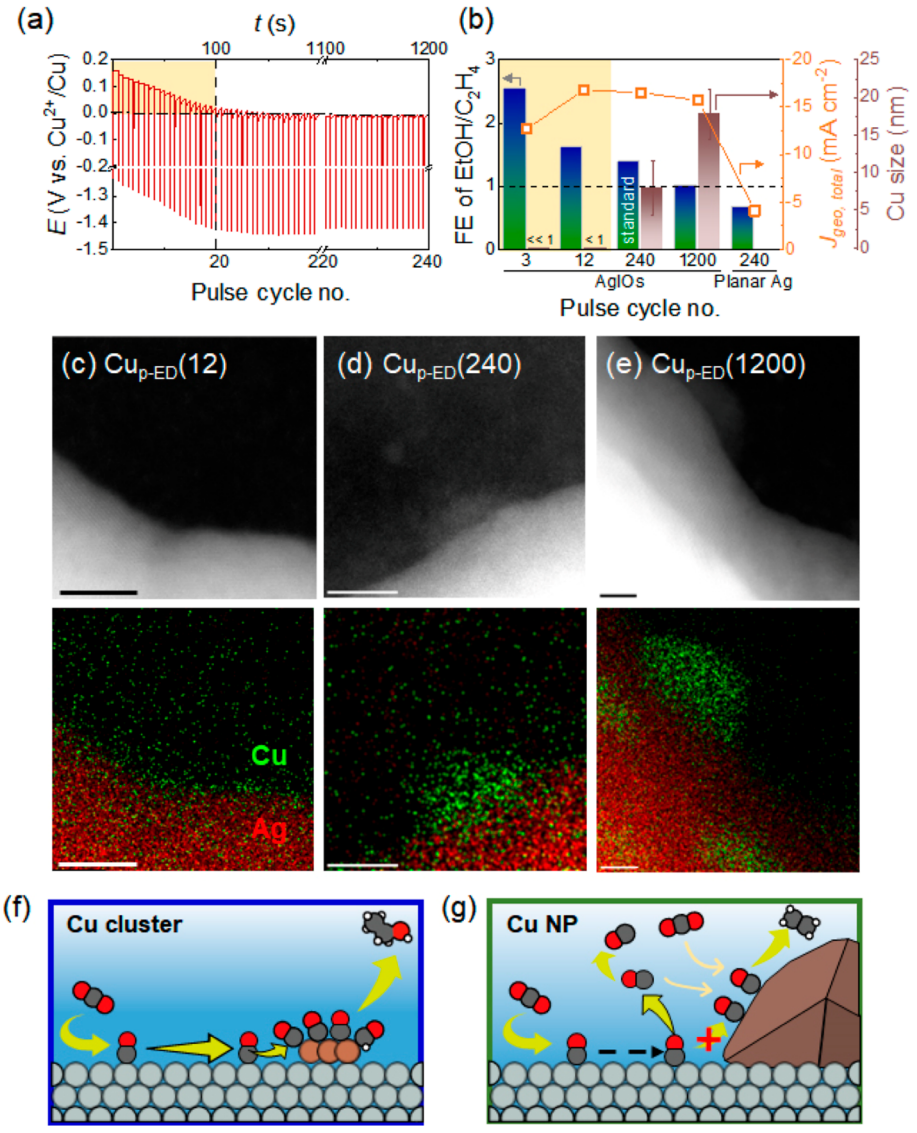

Figure 3. Controlling the deposited Cu quantity to selectively form Cu clusters and Cu NPs on AgIOs. (a) Representative potential profile for the p-ED process of Cu on AgIOs. The yellow region indicated incomplete Cu coverage on Ag due to a minute Cu deposition. (b) Comparative FE of EtOH to C_2H_4 ratio, $J_{geo,total}$, and average sizes of Cu from $Cu_{p\text{-}ED}$/AgIOs samples and $Cu_{p\text{-}ED}$/planar Ag. Different Cu sizes were controlled by p-ED cycles. The *e*-CO_2R was examined at −1.05 V for 3 h with a CO_2-saturated 0.2 M $KHCO_3$ solution, and Cu sizes were measured using STEM−EDS elemental mapping images. (c−e) (top) HAADF−STEM and (bottom) corresponding STEM−EDS elemental mapping images of $Cu_{p\text{-}ED}$/AgIOs after 3 h of *e*-CO_2R at −1.05 V with (c) 12, (d) 240, and (e) 1200 Cu p-ED cycles. The red and green indicate Ag and Cu, respectively, and the scale bars of (c−e) are 5 nm. Note that the net intensity maps in (c−e) are normalized for each element to better visualize the Ag layers and Cu NPs, and the maps do not directly represent the atomic fraction. (f−g) Schematic illustrations of (f) EtOH formation on the Cu cluster through surface-migrated CO and (g) C_2H_4 production on Cu NPs by solution-mediated CO migration or direct CO_2 reduction. Gray, brown, black, red, and white balls indicate Ag, Cu, C, O, and H atoms, respectively.

determined by XPS, which was distinct from that in bulk at 0.7/99.3 measured by inductively coupled plasma−optical emission spectroscopy (ICP−OES) (Tables S1 and S2). It evidenced surface deposition of the Cu layer.

The $Cu_{p\text{-}ED}(240)$/AgIOs structure comprised metallic Ag and various valence states of Cu. XPS and Auger spectra showed Ag^0 $3d_{3/2}$ and $3d_{5/2}$ spin−orbit coupling signals (Figures 1i and S3). For Cu, there were Cu^0, Cu^+, and Cu^{2+} states; the Cu^0 and Cu^+ signals were superimposed at ∼932.6 eV (orange) in XPS, and the small Cu^{2+} peak appeared at ∼934.6 eV (green) in the Cu $2p_{3/2}$ binding energy (BE) region (Figure 1j). The presence of predominant metallic Cu was validated by the rising-edge region at ∼8979 eV (1s → $4p_z$ transition of Cu^0) in the X-ray absorption near-edge structure (XANES) spectra (Figure 1k).[40] Consistently, k^2-weighted Fourier-transformed extended X-ray absorption fine structure (EXAFS) spectra exhibited the intense Cu^0−Cu^0 signal with a bond length of 2.18 Å (Figure 1l). In addition, the appearance of Cu−O with a length of 1.47 Å was associated with both Cu^+−O (referred to as Cu_2O at 1.41 Å) and Cu^{2+}−O (CuO at 1.50 Å). Therefore, all of the results demonstrate the formation of a Cu^0-dominant film with a mildly oxidized Cu surface.

Next, *e*-CO_2R was conducted on the as-prepared AgIOs and $Cu_{p\text{-}ED}(240)$/AgIOs. The *e*-CO_2R product selectivity was investigated by using a CO_2 gas-bubbled 0.2 M $KHCO_3$ aqueous solution in sandwich-type and two-compartment electrochemical cells. Ag is an excellent *e*-CO_2R catalyst for producing CO,[16,17,41] and Cu-free AgIOs showed exclusive CO

https://doi.org/10.1021/acscatal.3c03469
ACS Catal. 2024, 14, 3198−3207

Table 1. Details of $Cu_{p\text{-}ED}$/AgIOs Samples for $e\text{-}CO_2R$[a]

samples	usage/AgIOs thick-ness (μm)	p-ED cycle no. of Cu	Cu structure/size (nm)	J_{geo} (mA cm^{-1})	FE of EtOH (%)	FE of $EtOH/C_2H_4$
$Cu_{p\text{-}ED}(3)$/AgIOs	$e\text{-}CO_2R$ assess/4.5	3	cluster/no observation	−12.7	13.0	2.5
$Cu_{p\text{-}ED}(12)$/AgIOs		12	cluster/<1	−16.8	29.5	1.6
$Cu_{p\text{-}ED}(240)$/AgIOs		240	cluster + NPs/7.8 ± 3.9	−16.5[b]	28.8[b]	1.4[b]
$Cu_{p\text{-}ED}(1200)$/AgIOs		1200	NPs/18.0 ± 3.5	−15.7	18.9	1.0
$Cu_{p\text{-}ED}(10)$/$AgIOs_{-R}$	Raman/1.5	10	cluster	−8.6	24.3	1.8
$Cu_{p\text{-}ED}(80)$/$AgIOs_{-R}$		80	cluster + NPs	−9.1	26.0	1.7

[a]All of the CO_2R experiments were conducted at −1.05 V in 0.2 M $KHCO_3$ for 3 h. [b]The electrochemical results of $Cu_{p\text{-}ED}(240)$/AgIOs in Figure S11 deviate some from those in Figure 2c,d because the synthesis of $Cu_{p\text{-}ED}$/AgIOs is sensitive to the environment (temperature and humidity). However, their trends are consistent.

production (Figure 2a,b). With increasing overpotential, the geometric area-based current density of CO (indicated as $J_{geo,CO}$) linearly increased and approached −5.5 mA cm^{-2} at −1.05 V (vs reversible hydrogen electrode unless otherwise stated) with an FE of ∼95.1%.[42,43] In comparison, a planar Ag showed inferior $J_{geo,CO}$ at −1.50 mA cm^{-2} and lower FE for CO (FE_{CO}) at 76.3% (Figure S4). More importantly, the better CO conversion efficiency was linked to a lower H_2 evolution reaction (HER), demonstrating FE_{H2} values of ∼2% for AgIOs and 21.8% for planar Ag substrates (Figures 2b and S4). Because H^+ is depleted during CO formation (eq 1), vigorous CO generation increases the local pH and prevents HER.[42,43] It was more achieved in the confined space (AgIOs) compared to the open space (planar Ag).

$$CO_2 + 2H^+ + 2e^- \rightleftarrows CO + H_2O \quad (1)$$

Bearing in mind the Ag structure-dependent catalytic performance, we explored $Cu_{p\text{-}ED}$ on AgIOs and tested $e\text{-}CO_2R$ at the desired potentials for 3 h. With increasing cathodic potentials from −0.9 to −1.05 V, FE_{CO} decreased (∼39 to ∼13%), while the total FE for C_2 products, i.e., EtOH plus C_2H_4, was increased to >50% (Figure 2c,d, Table S3, S5, and S10). At −1.1 ∼ −1.15 V, CH_4 and H_2 were enhanced in reducing CO due to the significantly increased HER.[44] Thus, the optimal potential for C_2 production was −1.05 V, at which the total J_{geo} was −17.5 mA cm^{-2}. $Cu_{p\text{-}ED}(240)$/AgIOs provided a superior FE for EtOH (33.2%) compared to C_2H_4 (18.0%). This result was significantly different from that of CuIOs producing the predominant HER (FE_{H2}, ∼80%, Figure S5). After 20 h of $e\text{-}CO_2R$ at −1.05 V, FE for EtOH was still retained at 29% on $Cu_{p\text{-}ED}(240)$/AgIOs, indicating the long-term stability of EtOH active sites (Figure S6).

$Cu_{p\text{-}ED}(240)$/AgIOs remained robust and stable after $e\text{-}CO_2R$ at −1.05 V for 3 h (Figure S7), and there was no evidence of Cu loss during $e\text{-}CO_2R$ (ICP−OES analysis of the electrolyte solution; Table S2). However, the Cu began to be segregated, forming two types of structures, clusters (<1 nm size) and NPs, while Ag was exposed to the surface (Figure 2e−i). The subnanometer-scaled Cu clusters appeared in being osculated with Ag (green dots in Figure 2h), and the coexisting Cu NPs had an average diameter of 7.8 ± 3.9 nm (dashed box in Figure 2h and its high magnification image in Figure 2i, and other Cu NPs observations in Figure S8). XPS exhibited a negligible peak shift of Ag $3d_{3/2}$ and $3d_{5/2}$ before and after $e\text{-}CO_2R$ (Figure 2j), validating no CuAg alloy formation due to their immiscible property.[45] Additional Cu^{2+} signals emerging in XPS and Auger spectrum were attributed to the surface oxidation in the air during the analyses (Figure S9).[46] Correlated with $e\text{-}CO_2R$ results, both Cu and Ag served as catalysts for $e\text{-}CO_2R$,[17,21,47] where the Ag supplied CO to Cu.

We further tuned the Cu size distribution using the p-ED methods and identified a size-dependent Cu role for the C_2 process. The advantages of the p-ED were delicately controlling Cu quantity by cycling numbers and forming a uniform layer. When we monitored the OCP during the resting period of the p-ED process, it appeared to be >0 V vs Cu^{2+}/Cu before ∼20 cycles (yellow area in Figure 3a). It indicated a minute Cu deposition that partially covered the Ag surface. Such tiny Cu plating and subsequent $e\text{-}CO_2R$ formed small Cu clusters. Representatively, we adapted 3 and 12 $Cu_{p\text{-}ED}$ cycles, indicated as $Cu_{p\text{-}ED}(3)$/AgIOs and $Cu_{p\text{-}ED}(12)$/AgIOs, respectively, and observed Cu structures in multiple sites after $e\text{-}CO_2R$. Unfortunately, STEM−EDS did not clearly detect Cu in $Cu_{p\text{-}ED}(3)$/AgIOs due to the marginal amount and possibly very small size. However, it characterized well-distributed Cu clusters as subnanometer dots in $Cu_{p\text{-}ED}(12)$/AgIOs (Figures 3c and S10). More importantly, there was no Cu NP in the multiple sites of $Cu_{p\text{-}ED}(12)$/AgIOs, demonstrating the exclusive formation of Cu clusters from the low $Cu_{p\text{-}ED}$ cycle numbers. Correspondingly, the $e\text{-}CO_2R$ drastically increased FE_{EtOH} by Cu clusters; $Cu_{p\text{-}ED}(3)$/AgIOs had a $FE_{EtOH}/FE_{C_2H_4}$ ratio at 2.5 (Figure 3b). This remarkably high C_2 selectivity is likely attributed to the existing tiny Cu that was even not observed by the high-resolution STEM−EDS. However, the CO product was also predominant (FE_{CO} = 67%), and the total J_{geo} was low (Figure S11), because the absolute Cu amount was very low and the exposed Ag surface area was large. $Cu_{p\text{-}ED}(12)$/AgIOs provided the $FE_{EtOH}/FE_{C_2H_4}$ ratio at 1.6, which was higher than 1.4 for the $Cu_{p\text{-}ED}(240)$/AgIOs (Figure 3b). Further, the total J_{geo} and FE of C_2 species were comparable to that of the $Cu_{p\text{-}ED}(240)$/AgIOs despite a 20 times lower Cu quantity (Figure S11). Therefore, Cu clusters in AgIOs were active in C_2 production and preferentially formed EtOH, especially when the Cu size was smaller in lower $Cu_{p\text{-}ED}$ cycle numbers.

In contrast, when p-ED cycling numbers were increased, Cu was aggregated to be NPs, and the size was enlarged. Compared to the $Cu_{p\text{-}ED}(240)$/AgIOs with an average Cu NP diameter at 7.8 ± 3.9 nm (measured from total six areas) (Figures 3d and S8), 1200-times cycled p-ED, i.e., $Cu_{p\text{-}ED}(1200)$/AgIOs, had an average NP diameter at 18.0 ± 3.5 nm (measured from total eight areas) (Figures 3e and S12). STEM−EDS images showed a reduced Cu−Ag boundary and completely separated Ag and Cu NP domains (Figure 3d,e).

https://doi.org/10.1021/acscatal.3c03469
ACS Catal. 2024, 14, 3198−3207

For e-CO_2R, the $FE_{EtOH}/FE_{C_2H_4}$ ratio was 1.0 for $Cu_{p\text{-}ED}(1200)/AgIOs$, revealing an increase in the C_2H_4 portion (Figures 3b and S11). In addition, both FE and J_{geo} of C_2 species were decreased compared to those for the $Cu_{p\text{-}ED}(240)/AgIOs$ as the HER was enhanced. All $Cu_{p\text{-}ED}/AgIOs$ samples' structural sizes and e-CO_2R performances are summarized in Table 1.

Similar results also appeared from Cu particles synthesized by galvanostatic Cu plating on AgIOs (Figure S13). These Cu particles were hundreds of nanometers in size and had (100) facets, known as the active sites for C_2H_4.[6] In addition, when we applied the Cu p-ED method to planar Ag substrate, a hundred nanometers of Cu particles were deposited even after 240 cycles due to a low Ag surface area (Figures S14 and S15). This $Cu_{p\text{-}ED}$/planar Ag showed only <5% FE of C_2 at −1.05 V, and the FE ratio of EtOH to C_2H_4 was significantly low at 0.7 (Figure 3b, Tables S4, and S6).

Therefore, the overall results showed an apparent correlation between the Cu size and EtOH productivity. We attribute this transition to the CO delivery pathways and corresponding CO density on Cu. Because the Ag domains predominantly convert CO_2 to CO while weakly adsorbing CO, CO can move to Cu via two pathways: surface migration and solution-mediated transport. Previous computational simulation results revealed thermodynamic and kinetic preference for CO spillover, leading to stable *CO adsorption on Cu or Cu atomic layers on Ag.[48] Experimentally, the CO surface migration should be achieved when the spacing between Ag and Cu is short. Then CO is stuck at the abundant Cu−Ag boundary and migrates onto Cu. A continuous and rapid CO supply makes a dense CO population on Cu and promotes C−C coupling.[42,43] These conditions apply to subnanometre Cu clusters as they have a small height difference from the Ag surface and are widely distributed on the AgIOs (Figure 3f). High CO coverage on Cu can support the surface-migrating CO process, which will be discussed below by using vibrational spectroscopy. There are also unique features of the subnanometer Cu layer. It is reported that the ultrathin Cu layer on Ag modulates the Cu characters to Cu−Ag intermediate-like, which is favorable for CO and intermediates adsorption for EtOH production.[18,48,49] In addition, the subnanometer Cu has multiple and diverse binding sites, which are different from the typically well-defined active sites (e.g., low coordination sites) for C_2H_4.[49]

In sharp contrast, large Cu NPs have a few boundaries with Ag, which hinder the surface migration of CO (Figure 3g). Instead, solution-mediated CO transport can be predominant, which is a slow and site-selective process. Along with CO, Cu NPs also accommodate CO_2 and facilitate the entire e-CO_2R without any help from Ag. Compared to Cu clusters, the density of CO and CO_2 on the Cu NPs is low and concentrated on thermodynamically active sites to form C_2H_4.[47] Previous studies revealed that CO gas was mostly converted to C_2H_4 on Cu_2O/Ag nanostructures, where the solution-mediated CO adsorption took place.[18] In addition, the sole Cu[50] or Cu_2O nanocatalysts[51] also produced the significant C_2H_4 from CO_2 gas.

To shed light on the molecular catalytic reactions, *operando* electrochemical SHINERS was used for our catalysts. We prepared $Cu_{p\text{-}ED}/AgIOs_{-R}$, $Cu_{p\text{-}ED}$/planar Ag, and Cu film samples for the SHINERS analysis. For $Cu_{p\text{-}ED}/AgIOs_{-R}$, the thickness of the AgIOs (1.5 μm) was thinner than the above AgIOs (t = 4.5 μm) to reduce bubble generation. This thin AgIOs was indicated as $AgIOs_{-R}$. Subsequently, Cu coating was conducted by the p-ED method, and complete Cu coverage on $AgIOs_{-R}$ was achieved for five cycles (Figure S16). We fabricated $Cu_{p\text{-}ED}(10)/AgIOs_{-R}$ and $Cu_{p\text{-}ED}(80)/AgIOs_{-R}$ through 10 and 80 p-ED cycles. Both samples should form Cu clusters, but $Cu_{p\text{-}ED}(80)$ also developed NPs. The $Cu_{p\text{-}ED}(10)/AgIOs_{-R}$ evolved significant CO (FE_{CO} = 33.4% Tables S7−S9), a similar behavior to the above $Cu_{p\text{-}ED}(3)/AgIOs$ in Figure 3b. The FE ratio of EtOH to C_2H_4 was estimated to be 1.84 and 1.72, respectively, for 10 and 80 p-ED cycles (Figure S17), which were higher than the one of the above $Cu_{p\text{-}ED}(12)/AgIOs$ (1.6) in Figure 3b. $Cu_{p\text{-}ED}(80)/AgIOs_{-R}$ exhibited increased FEs for both EtOH and C_2H_4 compared to $Cu_{p\text{-}ED}(10)/AgIOs_{-R}$ because of increasing numbers of both Cu clusters and NPs. In comparison, 240 cycles of p-ED were applied for planar Ag, and an e-beam-evaporated Cu film was deposited on the Si wafer. Both $Cu_{p\text{-}ED}$/planar Ag and Cu films produced negligible EtOH and C_2H_4 (5−6% FE_{C2}), thus being categorized as C_2-inactive catalysts (Figure S17).

For SHINERS, Au (average d = ∼130 nm)@SiO_2 (average t = ∼5 nm) NPs were drop cast to cover the sample surface (Figure S18a,b).

The Au@SiO_2 NPs were inactive for the redox process (Figure S18c,d) but strengthened the surface plasmon resonance between the particles and sample junctions, which pronouncedly intensified Raman signals of the sample surface (Figure S19).[55] A 633 nm-laser and water-immersing objective lens were set up with a home-built single chamber spectro-electrochemical cell, and a CO_2-saturated 0.2 M $KHCO_3$ electrolyte solution was used with continuous CO_2 gas bubbling.

At the initial OCP, all Cu samples showed Cu_2O and $Cu(OH)_x$ bands at ∼530 cm^{-1} (Figure 4a−d and see assgined Raman modes in Table 2).[52,55] After stabilization at the OCP, the potential was applied from −1.1 to −0.4 V and rested at the OCP after terminating the e-CO_2R. This positive-potential scan showed reliable Raman signals at the initial high cathodic potentials (−0.9 ∼ −1.1 V) where the C_2 species were produced.

We first observed the essential atop-bound *CO bands on Cu, which were comprised of Cu−CO stretching (355−367 cm^{-1}) and Cu−CO rotating (283−300 cm^{-1}) bands (Figure 4a−d).[52,53] In particular, $Cu_{p\text{-}ED}(240)/AgIOs$ samples showed a redshift *CO stretching band (358.9 cm^{-1}) compared to the one for C_2-inactive catalysts ($Cu_{p\text{-}ED}$/planar Ag and Cu film) at −1.05 V (Figure 4e). It can explain the vicinal interactions between *CO molecules, possibly promoting the C−C coupling.[52] In addition, the active CO participating in the C_2 process was predicted from the estimation of *CO stretching to rotating intensity ratio in a previous report.[59] In our samples, the areal *CO intensity ratio increased as Cu film < $Cu_{p\text{-}ED}$/planar Ag < $Cu_{p\text{-}ED}/AgIOs_{-R}$ samples (Figures 4e and S20), which was consistent with the order of FE_{C2}. For $Cu_{p\text{-}ED}/AgIOs_{-R}$ samples, $Cu_{p\text{-}ED}(10)/AgIOs_{-R}$ had a higher *CO ratio than $Cu_{p\text{-}ED}(80)/AgIOs_{-R}$, demonstrating a higher population of active CO on $Cu_{p\text{-}ED}(10)$ and the favorable CO surface-migration process. Note that the FE_{C2} of $Cu_{p\text{-}ED}(10)/AgIOs_{-R}$ was lower than that of $Cu_{p\text{-}ED}(80)/AgIOs_{-R}$. It was attributed to the significant CO evolution from large $AgIOs_{-R}$ surface area (Figure S17).

Strong C≡O stretching mode also emerged at 2000−2100 cm^{-1} at the initial high cathodic potentials. Subsequently, the C≡O mode weakened at −0.4 ∼ −0.8 V as both *CO

https://doi.org/10.1021/acscatal.3c03469
ACS Catal. 2024, 14, 3198−3207

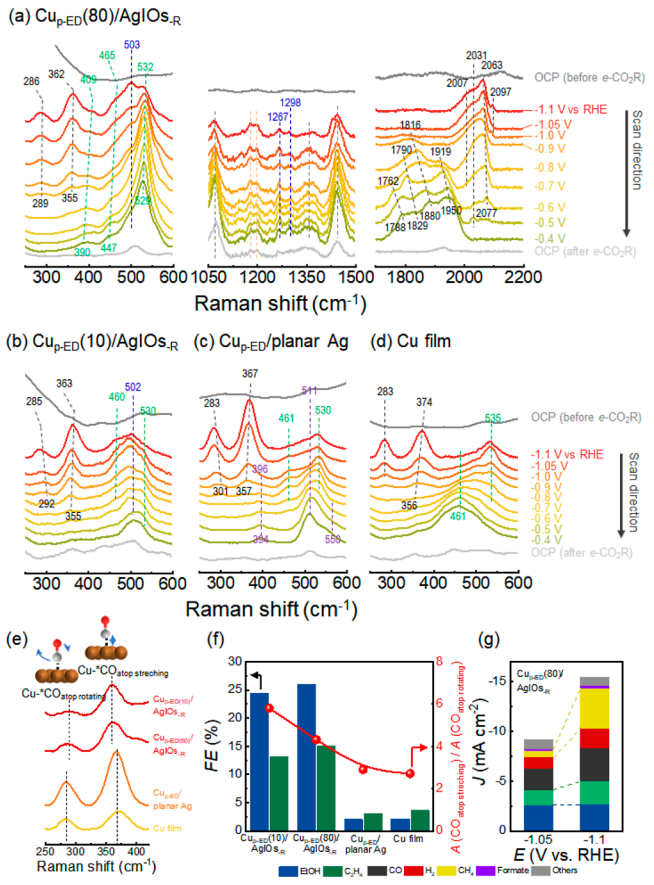

Figure 4. *Operando* electrochemical shell-isolated NP-enhanced Raman spectra (SHINERS) during *e*-CO_2R with a CO_2-saturated 0.2 M $KHCO_3$ solution. (a) Cu$_{p\text{-}ED}$(80)/AgIOs$_{-R}$, (b) Cu$_{p\text{-}ED}$(10)/AgIOs$_{-R}$, (c) Cu$_{p\text{-}ED}$/planar Ag, and (d) Cu film with positive-potential scan. The initial and terminating states were rested at the OCP (gray). Black, green, blue, and purple dashed lines indicate *CO on Cu, *OH or *O on Cu, *C_2 species on Cu, and *CO_2^- or *CO species on Ag, respectively. (e) Comparative Cu−CO atop stretching and rotating band modes for all samples. (f) FE of EtOH (blue) and C_2H_4 (green) linked to the areal Raman intensity ratio of atop-bound *CO stretching to rotating mode. (g) Total *e*-CO_2R current density of Cu$_{p\text{-}ED}$(80)/AgIOs$_{-R}$ samples at −1.05 and −1.1 V for 3 h.

stretching and rotating bands were attenuated (Figures 4a and S21). The decreased *CO coverage at the mild potential region caused the appearance of the bridge-bound C≡O at 1910−1950 cm^{-1} for Cu$_{p\text{-}ED}$/AgIOs$_{-R}$ samples.[13,52,60] In contrast, the bridge-bound CO appeared over the entire potential range on the C_2-inactive catalysts due to a low *CO coverage (Figure S21). Cu$_{p\text{-}ED}$(80)/AgIOs$_{-R}$, Cu$_{p\text{-}ED}$/planar Ag, and Cu film showed additional bands at 1760−1880 cm^{-1} in the mild potential region. It is assigned to *CO at defects, hollow sites, or undercoordinated sites of Cu NPs.[59] In contrast, such signals did not appear for Cu$_{p\text{-}ED}$(10)/AgIOs$_{-R}$, confirming the absence of the Cu NP. Instead, Cu$_{p\text{-}ED}$(10)/AgIOs$_{-R}$ exhibited a high wavenumber band at 2090−2118 cm^{-1} in −0.4 ∼ −0.9 V, likely associated with a weak *CO adsorption at the Cu−Ag boundary.

It is noted that high-sensitivity SHINERS also detects Ag−CO and Ag−CO_2^- signals. For example, Cu$_{p\text{-}ED}$/planar Ag, providing 33% FE_{CO}, showed weak *CO, strong out-of-plane wagging *OCO^-, and *COO^- band on a Ag at 394−396, 511, and 550 cm^{-1}, respectively, in −0.4 ∼ −0.6 V (Figure 4c, see

Table 2. Measured and Referred Raman Modes

Raman shift (cm^{-1})	Raman mode	references
283−300	Cu−*CO stretching	52,53
355−367	Cu−*CO rotating	
394−396	weak *CO on Ag	54
390−409	*O	55
460	bridged *OH	56
447−465	$Cu(OH)_2$ band	52,55
502−507	*C on Cu	53
511	strong out-of-plane wagging *OCO^- on Ag	54
530−532	atop-bound *OH	55,56
550	strong out-of-plane wagging *COO^- on Ag	54
1015−1020	bicarbonate anion, HCO_3^-	57,58
1060−1070	carbonate anion, CO_3^{2-}	53,58
1259−1280	C−O−H stretching of *OCCOH	55
1298	C−OH bending of *HOCCOH	
1760−1880	*CO at defects, hollow sites, or undercoordinated sites	59
1910−1950	bridge-bound *CO stretching	52,60
2000−2120	strong *CO stretching	58

similar signals on Cu-free AgIOs$_{-R}$ in Figure S22). In comparison, there was no Ag-related Raman band for Cu$_{p\text{-}ED}$(10)/AgIOs$_{-R}$ despite a similar FE_{CO} (33.4%). It verified dense CO coverage on Cu through the migration of CO from Ag.

Apart from *CO, *OH bands were notable for Cu$_{p\text{-}ED}$/AgIOs$_{-R}$ as the local pH was high. The Cu−OH bands comprised the atop-bound *OH at 530−532 cm^{-1} and the bridged *OH at 460 cm^{-1} (Figure 4a−d).[56] Cu$_{p\text{-}ED}$(80)/AgIOs$_{-R}$ had particularly profound Cu−OH signals and contained additional *O (390−409 cm^{-1}) and $Cu(OH)_2$ band (447−465 cm^{-1}) in the whole potential range. This OH adsorption on Cu should establish an equilibrium with OH dissolution in the high pH solution. It is noted that an apparent ratio between HCO_3^- at 1015−1020 cm^{-1} and CO_3^{2-} bands at 1060−1070 cm^{-1} also indicate the local pH degree.[61] However, these signals randomly fluctuated by introducing CO_2 gas bubbles in our cell configuration, and the HCO_3^- band overlapped with the residual PS bands in AgIOs$_{-R}$ (benzene ring breathe modes at 1000 and 1030 cm^{-1}) (Figures 4a and S21).

Taken together, the excess *CO on Cu and high local pH conditions promoted the C−C coupling process.[62,63] There are two possible coupling processes, *CO−*CH_x and *CO−*CHO.[28,55] The former is suggested as the main route for EtOH formation,[18,28,55] where the protonation of CO is prerequisite to form *CH_x. However, both Cu$_{p\text{-}ED}$/AgIOs$_{-R}$ samples did not show a *$COCH_x$ band (1302 cm^{-1}) (Figure S23). The C−H stretching mode of CH_x coupling (2800−3000 cm^{-1}) was not also clearly identified because residual chemicals from the AgIOs$_{-R}$ fabrication overlaid over 2800 cm^{-1} (Figure S24). As an alternative method of investigating the *CO−*CH_x route, we tried to enhance the J_{geo} of CH_4 by a negative potential shift and observe the corresponding J_{geo} of EtOH. Both J_{geo} should exhibit a positive correlation in this process. At −1.1 V, the increased protonation power resulted in increased yields of H_2, CH_4, and C_2H_4 on Cu$_{p\text{-}ED}$(80)/AgIOs$_{-R}$ (Figure 4g). However, J_{geo} of EtOH remained invariant compared to that at −1.05 V. A similar trend is also evident in Figure 2c, with a slight decrease in J_{geo} of EtOH.

https://doi.org/10.1021/acscatal.3c03469
ACS Catal. 2024, 14, 3198−3207

These results are unlikely to support the *CO−*CH_x coupling process for C−C coupling in $Cu_{p\text{-}ED}/AgIOs_{-R}$.

By contrast, all $Cu_{p\text{-}ED}/AgIOs_{-R}$ samples showed the notable C−O−H stretching of *OCCOH at 1259−1280 cm^{-1} regardless of the potential-scan directions (Figures 4a, S21a, and S23). $Cu_{p\text{-}ED}(80)/AgIOs_{-R}$ had an additional peak of 1298 cm^{-1} assigned to the C−OH bending of *HOCCOH. These signals demonstrated the prevalent *CO−*CHO coupling on the $Cu_{p\text{-}ED}/AgIOs_{-R}$ samples. Thus, both EtOH and C_2H_4 share the same initial intermediates *OCCOH. Further, the carbonaceous species (*C on Cu)-related Raman band[53] was remarkable at 502−507 cm^{-1}, which was only observed for the $Cu_{p\text{-}ED}/AgIOs_{-R}$ samples (Figures 4a,b, S21a, and S23). In particular, $Cu_{p\text{-}ED}(10)/AgIOs_{-R}$ showed more intense *C intensity than atop-bound *OH (530−532 cm^{-1}) at −0.9 ∼ −1.05 V, implying densely populated carbonaceous intermediates on Cu clusters. Presumably, various carbonaceous intermediates reside on Cu clusters after initial *CO−*CHO coupling. Thus, *operando* SHINER demonstrated the dense CO and carbonaceous intermediates coverage on Cu clusters, which influences the high selectivity of EtOH production.

CONCLUSIONS

In summary, the p-ED method regulated the quantity of Cu on the AgIOs and addressed Cu clusters as the core catalyst for EtOH. It caused high CO coverage on Cu clusters, and CO surface migrated from Ag as the spacing distance between Ag and Cu domains was short and their boundary was abundant. In contrast, Cu NPs increased C_2H_4 through solution-mediated CO migration or direct CO_2 reduction. *Operando* SHINERS validated high CO coverage on Cu clusters by the redshift of the *CO stretching mode and high areal intensity ratio of $Cu\text{-}CO_{streching}/Cu\text{-}CO_{rotating}$. In addition, the pronounced carbonaceous signal suggested a dense intermediate population of Cu clusters. SHINERS detected the *OCCOH band as the key intermediate regardless of Cu sizes, indicating the shared *CO−*CHO coupling process for both EtOH and C_2H_4 production. The critical factor for preferential EtOH was the high coverage of these intermediates on Cu. Our study revealed the pivotal role of subnanometer Cu cluster in porous Ag structure and guided catalyst design approaches toward improving EtOH selectivity for *e*-CO_2R.

ASSOCIATED CONTENT

Supporting Information

The Supporting Information is available free of charge at https://pubs.acs.org/doi/10.1021/acscatal.3c03469.

Additional SEM, XRD, XPS, HAADF−STEM/STEM−EDS, operando SHINERS, and electrochemical analysis data are included (PDF)

AUTHOR INFORMATION

Corresponding Authors

Yongsoo Yang − *Department of Physics, Korea Advanced Institute of Science and Technology (KAIST), Daejeon 34141, Republic of Korea; Graduate School of Semiconductor Technology, Korea Advanced Institute of Science and Technology (KAIST), Daejeon 34141, Republic of Korea;* orcid.org/0000-0001-8654-302X; Email: yongsoo.yang@kaist.ac.kr

Hye Ryung Byon − *Department of Chemistry, Korea Advanced Institute of Science and Technology (KAIST), Daejeon 34141, Republic of Korea;* orcid.org/0000-0003-3692-6713; Email: hrbyon@kaist.ac.kr

Authors

Jiwon Park − *Department of Chemistry, Korea Advanced Institute of Science and Technology (KAIST), Daejeon 34141, Republic of Korea;* orcid.org/0000-0002-2258-310X

Chaehwa Jeong − *Department of Physics, Korea Advanced Institute of Science and Technology (KAIST), Daejeon 34141, Republic of Korea;* orcid.org/0000-0001-9153-710X

Moony Na − *Department of Chemistry, Korea Advanced Institute of Science and Technology (KAIST), Daejeon 34141, Republic of Korea;* orcid.org/0000-0002-7172-9494

Yusik Oh − *Department of Chemistry, Korea Advanced Institute of Science and Technology (KAIST), Daejeon 34141, Republic of Korea;* orcid.org/0000-0003-1194-3330

Kug-Seung Lee − *Pohang Accelerator Laboratory, POSTECH, Pohang 37673, Republic of Korea;* orcid.org/0000-0002-7570-8404

Complete contact information is available at: https://pubs.acs.org/10.1021/acscatal.3c03469

Author Contributions

The manuscript was written through contributions of all authors. All authors have given approval to the final version of the manuscript.

Notes

The authors declare no competing financial interest.

ACKNOWLEDGMENTS

This work was supported by the National Research Foundation (NRF) of Korea grant, funded by the Korean Government (MSIT, NRF-2019R1A2C2007551, NRF-2020R1C1C1006239, NRF-2021R1A2C1011415, 2021R1A5A1030054, and RS-2023-00208179). The FIB sample preparation (FEI Helios G4), HAADF−STEM imaging (Titan Themis Z and Titan cubed G2 60-300), and STEM−EDS analysis (Titan Themis Z and Titan cubed G2 60-300) were conducted at the KAIST Analysis Center for Research Advancement (KARA) and DGIST Institute of Next-generation Semiconductor convergence Technology (INST). Excellent support by Tae Woo Lee, Jin-Seok Choi, Taehoon Cheon, and the staff of KARA and INST is gratefully acknowledged. The STEM data analyses were partially supported by the KAIST Quantum Research Core Facility Center (KBSI-NFEC grant funded by Korea government MSIT, PG2022004-09).

REFERENCES

(1) Kuhl, K. P.; Cave, E. R.; Abram, D. N.; Jaramillo, T. F. New insights into the electrochemical reduction of carbon dioxide on metallic copper surfaces. *Energy Environ. Sci.* **2012**, *5* (5), 7050−7059.

(2) Gao, D.; Arán-Ais, R. M.; Jeon, H. S.; Cuenya, B. R. Rational catalyst and electrolyte design for CO_2 electroreduction towards multicarbon products. *Nat. Catal.* **2019**, *2* (3), 198−210.

(3) Zheng, Y.; Vasileff, A.; Zhou, X.; Jiao, Y.; Jaroniec, M.; Qiao, S.-Z. Understanding the Roadmap for Electrochemical Reduction of CO_2 to Multi-Carbon Oxygenates and Hydrocarbons on Copper-Based Catalysts. *J. Am. Chem. Soc.* **2019**, *141* (19), 7646−7659.

(4) Nitopi, S.; Bertheussen, E.; Scott, S. B.; Liu, X.; Engstfeld, A. K.; Horch, S.; Seger, B.; Stephens, I. E. L.; Chan, K.; Hahn, C.; Nørskov, J. K.; Jaramillo, T. F.; Chorkendorff, I. Progress and Perspectives of Electrochemical CO_2 Reduction on Copper in Aqueous Electrolyte. *Chem. Rev.* **2019**, *119* (12), 7610−7672.
(5) Hori, Y. In *Modern Aspects of Electrochemistry*; Vayenas, C. G., White, R. E., Gamboa-Aldeco, M. E., Eds.; Springer New York: New York, NY, 2008; pp 89−189.
(6) Piqué, O.; Viñes, F.; Illas, F.; Calle-Vallejo, F. Elucidating the Structure of Ethanol-Producing Active Sites at Oxide-Derived Cu Electrocatalysts. *ACS Catal.* **2020**, *10* (18), 10488−10494.
(7) Xiao, H.; Goddard, W. A.; Cheng, T.; Liu, Y. Cu metal embedded in oxidized matrix catalyst to promote CO_2 activation and CO dimerization for electrochemical reduction of CO_2. *Proc. Natl. Acad. Sci. U.S.A.* **2017**, *114* (26), 6685−6688.
(8) Wei, X.; Yin, Z.; Lyu, K.; Li, Z.; Gong, J.; Wang, G.; Xiao, L.; Lu, J.; Zhuang, L. Highly Selective Reduction of CO_2 to C_{2+} Hydrocarbons at Copper/Polyaniline Interfaces. *ACS Catal.* **2020**, *10* (7), 4103−4111.
(9) Zhang, B.; Zhang, J.; Hua, M.; Wan, Q.; Su, Z.; Tan, X.; Liu, L.; Zhang, F.; Chen, G.; Tan, D.; Cheng, X.; Han, B.; Zheng, L.; Mo, G. Highly Electrocatalytic Ethylene Production from CO_2 on Nanodefective Cu Nanosheets. *J. Am. Chem. Soc.* **2020**, *142* (31), 13606−13613.
(10) Kim, C.; Cho, K. M.; Park, K.; Kim, J. Y.; Yun, G.-T.; Toma, F. M.; Gereige, I.; Jung, H.-T. Cu/Cu_2O Interconnected Porous Aerogel Catalyst for Highly Productive Electrosynthesis of Ethanol from CO_2. *Adv. Funct. Mater.* **2021**, *31* (32), 2102142.
(11) Gao, D.; Zegkinoglou, I.; Divins, N. J.; Scholten, F.; Sinev, I.; Grosse, P.; Cuenya, B. R. Plasma-Activated Copper Nanocube Catalysts for Efficient Carbon Dioxide Electroreduction to Hydrocarbons and Alcohols. *ACS Nano* **2017**, *11* (5), 4825−4831.
(12) Zhou, Y.; Che, F.; Liu, M.; Zou, C.; Liang, Z.; De Luna, P.; Yuan, H.; Li, J.; Wang, Z.; Xie, H.; Li, H.; Chen, P.; Bladt, E.; Quintero-Bermudez, R.; Sham, T.-K.; Bals, S.; Hofkens, J.; Sinton, D.; Chen, G.; Sargent, E. H. Dopant-induced electron localization drives CO_2 reduction to C_2 hydrocarbons. *Nat. Chem.* **2018**, *10* (9), 974−980.
(13) Wang, P.; Yang, H.; Tang, C.; Wu, Y.; Zheng, Y.; Cheng, T.; Davey, K.; Huang, X.; Qiao, S.-Z. Boosting electrocatalytic CO_2-to-ethanol production via asymmetric C-C coupling. *Nat. Commun.* **2022**, *13* (1), 3754.
(14) Morales-Guio, C. G.; Cave, E. R.; Nitopi, S. A.; Feaster, J. T.; Wang, L.; Kuhl, K. P.; Jackson, A.; Johnson, N. C.; Abram, D. N.; Hatsukade, T.; Hahn, C.; Jaramillo, T. F. Improved CO_2 reduction activity towards C_{2+} alcohols on a tandem gold on copper electrocatalyst. *Nat. Catal.* **2018**, *1* (10), 764−771.
(15) Gao, J.; Ren, D.; Guo, X.; Zakeeruddin, S. M.; Grätzel, M. Sequential catalysis enables enhanced C-C coupling towards multicarbon alkenes and alcohols in carbon dioxide reduction: a study on bifunctional Cu/Au electrocatalysts. *Faraday Discuss.* **2019**, *215* (0), 282−296.
(16) Hoang, T. T. H.; Verma, S.; Ma, S.; Fister, T. T.; Timoshenko, J.; Frenkel, A. I.; Kenis, P. J. A.; Gewirth, A. A. Nanoporous Copper-Silver Alloys by Additive-Controlled Electrodeposition for the Selective Electroreduction of CO_2 to Ethylene and Ethanol. *J. Am. Chem. Soc.* **2018**, *140* (17), 5791−5797.
(17) Wang, L.; Higgins, D. C.; Ji, Y.; Morales-Guio, C. G.; Chan, K.; Hahn, C.; Jaramillo, T. F. Selective reduction of CO to acetaldehyde with CuAg electrocatalysts. *Proc. Natl. Acad. Sci. U.S.A.* **2020**, *117* (23), 12572−12575.
(18) Ting, L. R. L.; Piqué, O.; Lim, S. Y.; Tanhaei, M.; Calle-Vallejo, F.; Yeo, B. S. Enhancing CO_2 Electroreduction to Ethanol on Copper-Silver Composites by Opening an Alternative Catalytic Pathway. *ACS Catal.* **2020**, *10* (7), 4059−4069.
(19) Lee, S.; Park, G.; Lee, J. Importance of Ag-Cu Biphasic Boundaries for Selective Electrochemical Reduction of CO_2 to Ethanol. *ACS Catal.* **2017**, *7* (12), 8594−8604.
(20) Ren, D.; Ang, B. S.-H.; Yeo, B. S. Tuning the Selectivity of Carbon Dioxide Electroreduction toward Ethanol on Oxide-Derived Cu_xZn Catalysts. *ACS Catal.* **2016**, *6* (12), 8239−8247.
(21) Lum, Y.; Ager, J. W. Sequential catalysis controls selectivity in electrochemical CO_2 reduction on Cu. *Energy Environ. Sci.* **2018**, *11* (10), 2935−2944.
(22) Iyengar, P.; Kolb, M. J.; Pankhurst, J.; Calle-Vallejo, F.; Buonsanti, R. Theory-Guided Enhancement of CO_2 Reduction to Ethanol on Ag-Cu Tandem Catalysts via Particle-Size Effects. *ACS Catal.* **2021**, *11* (21), 13330−13336.
(23) Li, J.; Xiong, H.; Liu, X.; Wu, D.; Su, D.; Xu, B.; Lu, Q. Weak CO binding sites induced by Cu-Ag interfaces promote CO electroreduction to multi-carbon liquid products. *Nat. Commun.* **2023**, *14* (1), 698.
(24) Gao, J.; Zhang, H.; Guo, X.; Luo, J.; Zakeeruddin, S. M.; Ren, D.; Grätzel, M. Selective C-C Coupling in Carbon Dioxide Electroreduction via Efficient Spillover of Intermediates As Supported by Operando Raman Spectroscopy. *J. Am. Chem. Soc.* **2019**, *141* (47), 18704−18714.
(25) Akter, T.; Pan, H.; Barile, C. J. Tandem Electrocatalytic CO_2 Reduction inside a Membrane with Enhanced Selectivity for Ethylene. *J. Phys. Chem. C* **2022**, *126* (24), 10045−10052.
(26) Zhang, T.; Bui, J. C.; Li, Z.; Bell, A. T.; Weber, A. Z.; Wu, J. Highly selective and productive reduction of carbon dioxide to multicarbon products via in situ CO management using segmented tandem electrodes. *Nat. Catal.* **2022**, *5* (3), 202−211.
(27) Chen, C.; Yan, X.; Liu, S.; Wu, Y.; Wan, Q.; Sun, X.; Zhu, Q.; Liu, H.; Ma, J.; Zheng, L.; Wu, H.; Han, B. Highly Efficient Electroreduction of CO_2 to C2+ Alcohols on Heterogeneous Dual Active Sites. *Angew. Chem., Int. Ed.* **2020**, *59* (38), 16459−16464.
(28) Wang, X.; Wang, Z.; de Arquer, F. P. G.; Dinh, C.-T.; Ozden, A.; Li, Y. C.; Nam, D.-H.; Li, J.; Liu, Y.-S.; Wicks, J.; Chen, Z.; Chi, M.; Chen, B.; Wang, Y.; Tam, J.; Howe, J. Y.; Proppe, A.; Todorović, P.; Li, F.; Zhuang, T.-T.; Gabardo, C. M.; Kirmani, A. R.; McCallum, C.; Hung, S.-F.; Lum, Y.; Luo, M.; Min, Y.; Xu, A.; O'Brien, C. P.; Stephen, B.; Sun, B.; Ip, A. H.; Richter, L. J.; Kelley, S. O.; Sinton, D.; Sargent, E. H. Efficient electrically powered CO_2-to-ethanol via suppression of deoxygenation. *Nat. Energy* **2020**, *5* (6), 478−486.
(29) Chen, C.; Yu, S.; Yang, Y.; Louisia, S.; Roh, I.; Jin, J.; Chen, S.; Chen, P.-C.; Shan, Y.; Yang, P. Exploration of the bio-analogous asymmetric C-C coupling mechanism in tandem CO_2 electroreduction. *Nat. Catal.* **2022**, *5* (10), 878−887.
(30) Li, J.; Li, C.; Hou, J.; Gao, W.; Chang, X.; Lu, Q.; Xu, B. Intercepting Elusive Intermediates in Cu-Mediated CO Electrochemical Reduction with Alkyl Species. *J. Am. Chem. Soc.* **2022**, *144* (44), 20495−20506.
(31) Sand, H. J. S. III. On the concentration at the electrodes in a solution, with special reference to the liberation of hydrogen by electrolysis of a mixture of copper sulphate and sulphuric acid. *London, Edinburgh Dublin Phil. Mag. J. Sci.* **1901**, *1* (1), 45−79.
(32) Chandrasekar, M. S.; Pushpavanam, M. Pulse and pulse reverse plating—Conceptual, advantages and applications. *Electrochim. Acta* **2008**, *53* (8), 3313−3322.
(33) Qiu, Y.-L.; Zhong, H.-X.; Zhang, T.-T.; Xu, W.-B.; Li, X.-F.; Zhang, H.-M. Copper Electrode Fabricated via Pulse Electrodeposition: Toward High Methane Selectivity and Activity for CO_2 Electroreduction. *ACS Catal.* **2017**, *7* (9), 6302−6310.
(34) Song, H.; Im, M.; Song, J. T.; Lim, J.-A.; Kim, B.-S.; Kwon, Y.; Ryu, S.; Oh, J. Effect of mass transfer and kinetics in ordered Cu-mesostructures for electrochemical CO_2 reduction. *Appl. Catal., B* **2018**, *232*, 391−396.
(35) Hall, A. S.; Yoon, Y.; Wuttig, A.; Surendranath, Y. Mesostructure-Induced Selectivity in CO_2 Reduction Catalysis. *J. Am. Chem. Soc.* **2015**, *137* (47), 14834−14837.
(36) Gaulding, E. A.; Liu, G.; Chen, C. T.; Löbbert, L.; Li, A.; Segev, G.; Eichhorn, J.; Aloni, S.; Schwartzberg, A. M.; Sharp, I. D.; Toma, F. M. Fabrication and optical characterization of polystyrene opal templates for the synthesis of scalable, nanoporous (photo)-

https://doi.org/10.1021/acscatal.3c03469
ACS Catal. 2024, 14, 3198−3207

electrocatalytic materials by electrodeposition. *J. Mater. Chem. A* **2017**, *5* (23), 11601−11614.
(37) Hu, C.-C.; Wu, C.-M. Effects of deposition modes on the microstructure of copper deposits from an acidic sulfate bath. *Surf. Coat. Technol.* **2003**, *176* (1), 75−83.
(38) Xing, S.; Zanella, C.; Deflorian, F. Effect of pulse current on the electrodeposition of copper from choline chloride-ethylene glycol. *J. Solid State Electrochem.* **2014**, *18* (6), 1657−1663.
(39) Pei, A.; Zheng, G.; Shi, F.; Li, Y.; Cui, Y. Nanoscale Nucleation and Growth of Electrodeposited Lithium Metal. *Nano Lett.* **2017**, *17* (2), 1132−1139.
(40) Oh, Y.; Park, J.; Kim, Y.; Shim, M.; Kim, T.-S.; Park, J. Y.; Byon, H. R. Coverage of capping ligands determining the selectivity of multi-carbon products and morphological evolution of Cu nano-catalysts in electrochemical reduction of CO_2. *J. Mater. Chem. A* **2021**, *9* (18), 11210−11218.
(41) Kottakkat, T.; Klingan, K.; Jiang, S.; Jovanov, Z. P.; Davies, V. H.; El-Nagar, G. A. M.; Dau, H.; Roth, C. Electrodeposited AgCu Foam Catalysts for Enhanced Reduction of CO_2 to CO. *ACS Appl. Mater. Interfaces* **2019**, *11* (16), 14734−14744.
(42) Suter, S.; Haussener, S. Optimizing mesostructured silver catalysts for selective carbon dioxide conversion into fuels. *Energy Environ. Sci.* **2019**, *12* (5), 1668−1678.
(43) Yoon, Y.; Hall, A. S.; Surendranath, Y. Tuning of Silver Catalyst Mesostructure Promotes Selective Carbon Dioxide Conversion into Fuels. *Angew. Chem., Int. Ed.* **2016**, *55* (49), 15282−15286.
(44) Iyengar, P.; Kolb, M. J.; Pankhurst, J. R.; Calle-Vallejo, F.; Buonsanti, R. Elucidating the Facet-Dependent Selectivity for CO_2 Electroreduction to Ethanol of Cu-Ag Tandem Catalysts. *ACS Catal.* **2021**, *11* (8), 4456−4463.
(45) Subramanian, P. R.; Perepezko, J. H. The ag-cu (silver-copper) system. *J. Phase Equilib.* **1993**, *14* (1), 62−75.
(46) Li, Y.; Kim, D.; Louisia, S.; Xie, C.; Kong, Q.; Yu, S.; Lin, T.; Aloni, S.; Fakra, S. C.; Yang, P. Electrochemically scrambled nanocrystals are catalytically active for CO_2-to-multicarbons. *Proc. Natl. Acad. Sci. U.S.A.* **2020**, *117* (17), 9194−9201.
(47) Liu, Y.; Qiu, H.; Li, J.; Guo, L.; Ager, J. W. Tandem Electrocatalytic CO_2 Reduction with Efficient Intermediate Conversion over Pyramid-Textured Cu-Ag Catalysts. *ACS Appl. Mater. Interfaces* **2021**, *13* (34), 40513−40521.
(48) Zhang, H.; Chang, X.; Chen, J. G.; Goddard, W. A.; Xu, B.; Cheng, M.-J.; Lu, Q. Computational and experimental demonstrations of one-pot tandem catalysis for electrochemical carbon dioxide reduction to methane. *Nat. Commun.* **2019**, *10* (1), 3340.
(49) Li, Y. C.; Wang, Z.; Yuan, T.; Nam, D.-H.; Luo, M.; Wicks, J.; Chen, B.; Li, J.; Li, F.; de Arquer, F. P. G.; Wang, Y.; Dinh, C.-T.; Voznyy, O.; Sinton, D.; Sargent, E. H. Binding Site Diversity Promotes CO_2 Electroreduction to Ethanol. *J. Am. Chem. Soc.* **2019**, *141* (21), 8584−8591.
(50) Kim, D.; Kley, C. S.; Li, Y.; Yang, P. Copper nanoparticle ensembles for selective electroreduction of CO_2 to C_2-C_3 products. *Proc. Natl. Acad. Sci. U.S.A.* **2017**, *114* (40), 10560−10565.
(51) Jung, H.; Lee, S. Y.; Lee, C. W.; Cho, M. K.; Won, D. H.; Kim, C.; Oh, H.-S.; Min, B. K.; Hwang, Y. J. Electrochemical Fragmentation of Cu_2O Nanoparticles Enhancing Selective C-C Coupling from CO_2 Reduction Reaction. *J. Am. Chem. Soc.* **2019**, *141* (11), 4624−4633.
(52) Zhan, C.; Dattila, F.; Rettenmaier, C.; Bergmann, A.; Kühl, S.; García-Muelas, R.; López, N.; Cuenya, B. R. Revealing the CO Coverage-Driven C-C Coupling Mechanism for Electrochemical CO_2 Reduction on Cu_2O Nanocubes via Operando Raman Spectroscopy. *ACS Catal.* **2021**, *11* (13), 7694−7701.
(53) Moradzaman, M.; Mul, G. In Situ Raman Study of Potential-Dependent Surface Adsorbed Carbonate, CO, OH, and C Species on Cu Electrodes During Electrochemical Reduction of CO_2. *Chemelectrochem* **2021**, *8* (8), 1478−1485.
(54) Shan, W.; Liu, R.; Zhao, H.; He, Z.; Lai, Y.; Li, S.; He, G.; Liu, J. In Situ Surface-Enhanced Raman Spectroscopic Evidence on the Origin of Selectivity in CO_2 Electrocatalytic Reduction. *ACS Nano* **2020**, *14* (9), 11363−11372.
(55) Shao, F.; Wong, J. K.; Low, Q. H.; Iannuzzi, M.; Li, J.; Lan, J. In situ spectroelectrochemical probing of CO redox landscape on copper single-crystal surfaces. *Proc. Natl. Acad. Sci. U.S.A.* **2022**, *119* (29), No. e2118166119.
(56) Niaura, G. Surface-enhanced Raman spectroscopic observation of two kinds of adsorbed OH^- ions at copper electrode. *Electrochim. Acta* **2000**, *45* (21), 3507−3519.
(57) Lu, X.; Zhu, C.; Wu, Z.; Xuan, J.; Francisco, J. S.; Wang, H. In Situ Observation of the pH Gradient near the Gas Diffusion Electrode of CO_2 Reduction in Alkaline Electrolyte. *J. Am. Chem. Soc.* **2020**, *142* (36), 15438−15444.
(58) He, M.; Chang, X.; Chao, T.-H.; Li, C.; Goddard, W. A.; Cheng, M.-J.; Xu, B.; Lu, Q. Selective Enhancement of Methane Formation in Electrochemical CO_2 Reduction Enabled by a Raman-Inactive Oxygen-Containing Species on Cu. *ACS Catal.* **2022**, *12* (10), 6036−6046.
(59) Gunathunge, C. M.; Ovalle, V. J.; Li, Y.; Janik, M. J.; Waegele, M. M. Existence of an Electrochemically Inert CO Population on Cu Electrodes in Alkaline pH. *ACS Catal.* **2018**, *8* (8), 7507−7516.
(60) Shen, H.; Wang, Y.; Chakraborty, T.; Zhou, G.; Wang, C.; Fu, X.; Wang, Y.; Zhang, J.; Li, C.; Xu, F.; Cao, L.; Mueller, T.; Wang, C. Asymmetrical C-C Coupling for Electroreduction of CO on Bimetallic Cu-Pd Catalysts. *ACS Catal.* **2022**, *12* (9), 5275−5283.
(61) Henckel, D. A.; Counihan, M. J.; Holmes, H. E.; Chen, X.; Nwabara, U. O.; Verma, S.; Rodríguez-López, J.; Kenis, P. J. A.; Gewirth, A. A. Potential Dependence of the Local pH in a CO_2 Reduction Electrolyzer. *ACS Catal.* **2021**, *11* (1), 255−263.
(62) Iijima, G.; Inomata, T.; Yamaguchi, H.; Ito, M.; Masuda, H. Role of a Hydroxide Layer on Cu Electrodes in Electrochemical CO_2 Reduction. *ACS Catal.* **2019**, *9* (7), 6305−6319.
(63) Le Duff, C. S.; Lawrence, M. J.; Rodriguez, P. Role of the Adsorbed Oxygen Species in the Selective Electrochemical Reduction of CO_2 to Alcohols and Carbonyls on Copper Electrodes. *Angew. Chem., Int. Ed.* **2017**, *56* (42), 12919−12924.

https://doi.org/10.1021/acscatal.3c03469
ACS Catal. 2024, 14, 3198−3207